Research Square

Preprints are preliminary reports that have not undergone peer review.
They should not be considered conclusive, used to inform clinical practice,
or referenced by the media as validated information.

Ultra-High Sensitivity Terahertz Dual-Parameter Sensing Based on Eccentric-Core Photonic Crystal Fiber

Yanyan Wang
Nanjing University of Posts and Telecommunications
WeiHua Shi
shiwh@njupt.edu.cn

Nanjing University of Posts and Telecommunications
Hui Zhao
Nanjing University of Posts and Telecommunications
Xiling Zheng
Nanjing University of Posts and Telecommunications

Research Article

Keywords: Photonic crystal fiber, Terahertz, Surface plasmon resonance, Directional coupling, Dual-parameter sensing

Posted Date: September 8th, 2026

DOI: https://doi.org/10.21203/rs.3.rs-10341180/v1

License: This work is licensed under a Creative Commons Attribution 4.0 International License.
Read Full License

Additional Declarations: No competing interests reported.

Version of Record: A version of this preprint was published at Plasmonics on October 5th, 2026. See the published version at https://doi.org/10.1007/s11468-026-03493-y.

Ultra-High Sensitivity Terahertz Dual-Parameter Sensing Based on Eccentric-Core Photonic Crystal Fiber

Yanyan Wang[1] · Weihua Shi[1] · Hui Zhao[1] · Xiling Zheng[1]

Abstract

To overcome the temperature cross-sensitivity common in single-parameter sensing, as well as the insufficient sensitivity and limited penetration depth of conventional near- and mid-infrared sensors, this paper proposes an ultrahigh-sensitivity terahertz (THz) dual-parameter sensor based on an eccentric photonic crystal fiber (PCF). The proposed structure features an outer surface coated with a molybdenum disulfide (MoS_2) layer, which creates a surface plasmon resonance (SPR) sensing channel specifically designed for detecting refractive index. Simultaneously, a thermosensitive liquid is filled into the central air holes of the PCF, forming a directional coupling sensing channel dedicated to precise temperature measurement. Simulation results demonstrate that the refractive index sensing channel and the temperature sensing channel can operate with a high degree of independence. Within the refractive index range of 1.33–1.38, a refractive index sensitivity of up to 1080.0 μm/RIU is achieved, with a full width at half maximum (FWHM) of 10.7 μm; over the temperature range of –20 to 40 °C, the temperature sensitivity reaches 0.85 μm/°C, and a relatively narrow FWHM of 0.4 μm is obtained. In addition, benefiting from the characteristics of terahertz-band plasmon-like resonance, the sensor can theoretically achieve a penetration depth of tens of micrometers. With ultrahigh sensitivity and large penetration depth, the proposed dual-parameter sensor has great potential for biochemical sensing and trace detection applications.

Keywords Photonic crystal fiber · Terahertz · Surface plasmon resonance · Directional coupling · Dual-parameter sensing

Introduction

With the advancement of sensing requirements, traditional single-parameter sensors struggle to meet the monitoring demands of complex systems. For instance, in biomedical detection, temperature fluctuations can affect the concentration analysis of targets such as nucleic acids and proteins. Similarly, in industrial and environmental monitoring, the refractive index of wastewater is influenced by both pollutant concentration and temperature. Such temperature-induced cross-sensitivity is often overlooked by conventional sensors, leading to reduced measurement reliability. This limitation drives the development of dual-parameter sensing technologies. PCF has emerged as a promising solution, providing high-sensitivity dual-parameter sensing with design flexibility and compatibility across various sensing mechanisms. Current PCF-based dual-parameter sensors primarily operate within the visible-to-infrared range, achieving sensitivities near 10^4 nm/RIU with micrometer-scale air holes [1–3]. However, the constraints on penetration depth are overlooked. Typically, near- to mid-infrared sensors are limited to a penetration depth of approximately 100 nm[4]. However, advanced trace detection requires sensitivities of 10^5–10^6 nm/RIU or higher [5-7]. Moreover, biomedical detection of biomacromolecules necessitates a penetration depth of 10–60 μm. This range is crucial for effectively monitoring weak signals and the dynamics of micron-sized particles, such as proteins and bacteria, within the sensing layer [4]. Consequently, existing PCF-based sensors fail to meet the demanding requirements for both sensitivity and penetration depth.

To address the challenges, the field of fiber sensing has expanded into the THz band. Compared with the visible and mid-infrared bands, the THz band has a significantly longer wavelength, resulting in two major advantages. Firstly, variations in the same refractive index lead to greater wavevector mismatch and resonance wavelength shifts, thereby enabling ultrahigh wavelength sensitivity. Secondly, both the evanescent field penetration depth and the skin depth increase considerably, reaching a detection depth of several tens of micrometers [4]. This enhanced depth is particularly suitable for detecting biomacromolecules and microparticles. In addition, the THz band possesses unique properties, including low photon energy, high penetration depth, ultrashort pulse durations, and strong spatial coherence [8]. These characteristics enable a wide range of applications, from non-destructive testing to label-free, non-invasive molecular detection. Furthermore, the air-hole dimensions in THz microstructured fibers are typically on the order of several hundred micrometers [9–13], reducing fabrication complexity while enhancing structural stability. These attributes have collectively driven extensive research in THz sensing, resulting in a series of studies in both single-parameter and dual-parameter sensors. For single-parameter sensing, in 2021, Liu et al. [9] proposed a MoS_2-based D-shaped SPR-PCF biosensor, achieving an average sensitivity of 715.59 μm/RIU. In 2024, He et al. [10] reported a graphene-coated outer-surface PCF-SPR sensor with an average sensitivity of 967.4 μm/RIU and a maximum sensitivity of 4254.11 μm/RIU. For dual-parameter sensing, in 2022, Liu et al. [11] coated PVDF on a circular PCF, achieving average sensitivities of 110 and 102.5 μm/RIU. In 2025, Xue et al. [12] designed a dual D-shaped SPR-PCF sensor; the upper channel achieved a maximum wavelength sensitivity of approximately 153.83 μm/RIU, while the lower channel, enhanced with ZnO sensitization, reached a

✉ WeiHua Shi
shiwh@njupt.edu.cn

[1] College of Electronic and Optical Engineering, College of Flexible Electronics (Future Technology), Nanjing University of Posts and Telecommunications, Nanjing, Jiangsu 210023, China

maximum sensitivity of 602.52 μm/RIU and an average of approximately 200 μm/RIU. In 2026, Yin et al. [13] proposed a MoS_2-based SPR-MOF sensor, achieving maximum wavelength sensitivities of 222.22 μm/RIU and 2385.72 μm/RIU.

In summary, the literature has employed various fiber types, plasmonic materials, and coating methods to realize dual-parameter sensing via a single SPR in the THz regime. The main fiber structure is PCF, which offers structural design flexibility. The primary plasmonic materials are graphene, MoS_2, and PVDF, which enable strong field confinement and high sensitivity in the THz regime. Coating methods include internal and external approaches, with the circular external structure simplifying fabrication while preserving integrity. Overall, these advances have significantly improved THz dual-parameter sensing. Overall, these approaches have led to significant progress in THz dual-parameter sensing. However, research in this area still faces challenges. Some structures provide independent channels without crosstalk but lack sufficient sensitivity. Others achieve high sensitivity and linearity but suffer from cross-sensitivity, requiring matrix demodulation.

To address these challenges, this paper proposes a novel THz eccentric-core PCF structure for dual-parameter sensing. To achieve this, the external coating activates the SPR effect. Meanwhile, filling the central air hole with a temperature-sensitive material generates the directional coupling effect. Together, these two mechanisms enable independent detection of refractive index and temperature. To further enhance performance, the asymmetric eccentric-core design reduces the distance between the fiber core and the sensing layer, overcoming the typical insufficient coupling strength associated with external coatings. The design offers high sensitivity and a large penetration depth, while eliminating cross-sensitivity through multi-mechanism interactions. Therefore, this sensor holds significant potential for applications in biochemical analysis, cell detection, and trace monitoring.

Theoretical Sensing Analysis

Structure Design and Simulation Model

Taking advantage of the long wavelength of the THz band, a THz fiber sensor with ultrahigh sensitivity, large detection depth, and substantial geometric dimensions is proposed, as illustrated in Fig. 1. In this structure, an external coating on the circular PCF cladding enables SPR sensing. To overcome the coupling deficiency caused by the external coating, the design removes one air hole from the second ring and reduces the size of the air holes between the core and the plasmonic layer. These modifications create an asymmetric eccentric-core design, enabling efficient coupling between the THz core mode and surface plasmon polaritons (SPP). A temperature-sensitive liquid fills the central air hole. This liquid creates a directional coupling mechanism that enables simultaneous monitoring of environmental temperature. This architecture provides a structural foundation for building THz sensors with ultrahigh sensitivity and significant detection depth. It also enables independent dual-parameter sensing of refractive index and temperature on a single fiber platform.

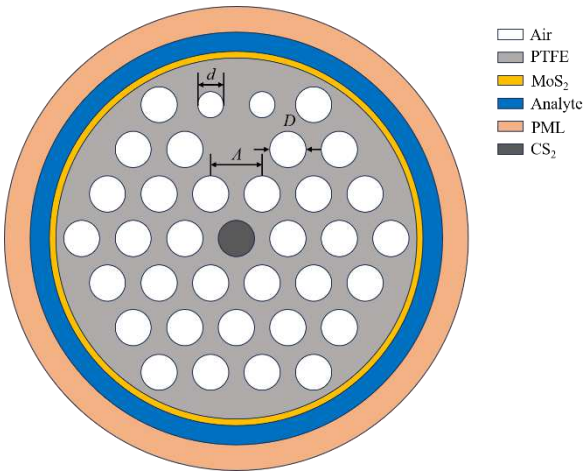


Fig.1 Cross-section of the designed eccentric-core PCF

As shown in Fig. 1, the air holes in the cladding of the PCF are arranged in a hexagonal pattern. The lattice pitch is set to Λ. The diameters of the two air holes near the excitation layer are defined as d, and the remaining air holes as D. An excitation layer of 2H-MoS_2 with thickness t is adopted. Polytetrafluoroethylene (PTFE) is selected as the fiber substrate due to its lower refractive index (n≈1.45) [14]. Compared with common materials such as Zeonex and Topas (n≈1.53), PTFE enables sensing over a wider range of refractive indices. Moreover, PTFE benefits from mature processing technology, ensuring high fabrication yield and uniformity. In the range of 0.1–3 THz, PTFE exhibits low dispersion [14–16], and its refractive index is 1.447. The 2H-MoS_2 layer is employed because its high specific surface area enhances biosensing performance. Its frequency-dependent dielectric constant follows the Drude model [9,12]:

$$\varepsilon = \varepsilon_{\infty} - \frac{\omega_p^2}{\omega^2 - i\Gamma\omega} \tag{1}$$

Where $\varepsilon_{\infty} = 11.475$ is the dielectric constant at high frequency limit, $\omega_p = \sqrt{Ne^2/(\varepsilon_0 m^*)}$, is the plasma frequency, and $\Gamma = e^2/(m^*\mu_c)$ is the damping rate of the carriers. Here, e is the charge of an electron, m^* is the effective mass of the carriers with me being the mass of an electron, $m^*=0.58m_e$, μ_c is the carrier mobility, and N is the intrinsic carrier density. We assume $\Gamma/2\pi=1.17THz$, which was retrieved from experimental data. here, we choose the MoS_2 crystal which intrinsic carrier density $N=5\times10^{16}$ cm^{-3}. Carbon disulfide (CS_2) is employed as the temperature-sensitive liquid. Based on the Debye model[17], its refractive index at room temperature (defined as 23°C in this work) and at a frequency of 1 THz is determined to be 1.5867, and the thermo-optic coefficient (dn/dT) is determined to be $7.594\times10^{-4}°C^{-1}$[18].

The PTFE tubing with air holes can be extruded through a hot pressurized die [14], which maintains the air hole structures over long tube lengths. To ensure homogeneous filling, the temperature-sensitive liquid is infiltrated into the air holes by pressure-assisted injection or low-pressure suction [19]. Finally, we deposit the MoS_2 layer on the PCF's external surface via the liquid transfer method [20].

Mode Analysis and Coupling Mechanism

The performance of this sensing structure is numerically analyzed by the finite element method. The x-direction is chosen as the polarization direction.

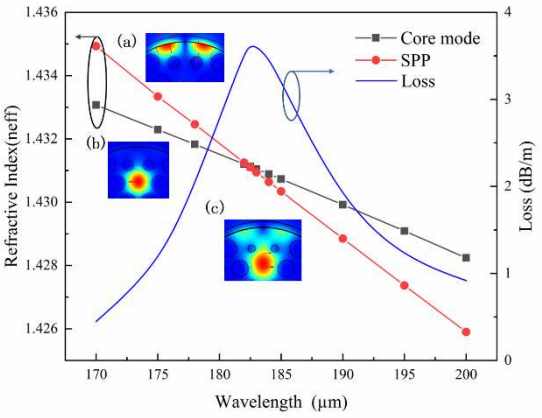


Fig.2 Dispersion lines of core-mode and SPP mode with the loss spectrum. The inserts a, b, and c are the optical field distribution at different ranges.

First, we investigate the refractive index sensing characteristics based on the SPR effect. Figure 2 shows the dispersion relations of the core mode (black line) and the SPP mode (red line), and the loss spectrum of the core mode (blue line) when n_1=1.36 and T=20°C. Away from the phase match point, Fig. 2(a) and 2(b) show the mode field distributions of the SPP and eccentric core modes, respectively. At the phase match point, the dispersion curves of the two modes intersect. Here, partial energy from the eccentric core mode couples into the SPP mode, producing a peak in the loss curve. Fig. 2(c) illustrates the corresponding mode field distribution. As the wavelength increases further, the energy of the eccentric core and SPP modes returns to their respective regions. Throughout this process, the two modes do not fully exchange energy. This behavior is incomplete coupling (the crossing effect).

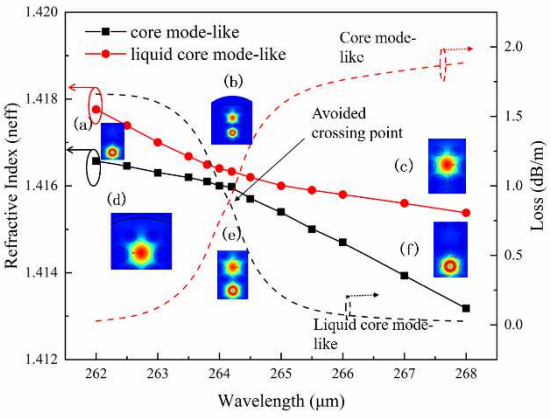


Fig.3 Dispersion lines of core-mode-like and liquid core mode-like with the loss spectrum. The inserts a, b, c, d, e, and f are the optical field distribution at different ranges

Subsequently, we investigated the temperature sensing characteristics based on the directional coupling effect. Figure 3 shows the wavelength-dependent dispersion and loss curves of the two new modes at 20 °C with an analyte refractive index of n_1=1.36. The two phase-matched modes couple and split into two new modes: a core-like mode and a liquid-core-like mode. For the liquid-core-like mode, the field is mainly confined within the liquid core region at shorter wavelengths Fig. 3(a). As the wavelength increases, more field energy transfers from the liquid core to the eccentric core region. At the coupling point, the field intensities in the liquid core and the eccentric core region become equal Fig. 3(b). At longer wavelengths, nearly all the field energy transfers from the liquid core to the eccentric core region Fig. (3c). The evolution of the core-like mode follows the opposite trend.

The loss curves of the two newly formed modes intersect in Fig. 3. In other words, the losses of the two modes tend to become equal at the avoided crossing point. This behavior is a complete coupling (avoided crossing effect). When tracing the original eigenmodes, the loss curve of the liquid-core mode reaches a peak at the avoided crossing point.

Coupled-mode theory[21] describes both the SPR between the SPP and core modes and the directional coupling between the core and liquid-core modes. For these coupled modes, we assume the propagation constant of the new coupling mode is β :

$$\beta_{\pm} = \beta_{ave} \pm \sqrt{\delta^2 + \kappa^2} \tag{2}$$

Where $\beta_{ave} = (\beta_1 + \beta_2)/2$, and $\delta = (\beta_1 - \beta_2)/2$. β_1 and β_2 are the propagation constants of core and SPP or liquid core mode, κ is the coupling strength. The two modes are leaky because their real parts of the mode refractive index are lower than that of the background material. For leaky modes, β_1 and β_2 are complex. Therefore, δ can be represented by $\delta = \delta_r + i\delta_i$. The real parts of propagation constants of the core and SPP mode are equal as the phase matching condition is satisfied; therefore, $\delta_r = 0$. Then, we can get the equation

$$\delta^2 + \kappa^2 = -\delta_i^2 + \kappa^2 \tag{3}$$

When $\kappa < \delta_i$, the real parts of β_+ and β_- are different, the imaginary parts of β_+ and β_- are equal, corresponding to non-intersecting dispersion curves at the phase-matching point, while loss curves intersect, complete coupling occurs between the two leaky modes. This case corresponds to Fig. 3. Conversely, when $\kappa > \delta_i$, β_+ and β_- share the same real part but distinct imaginary parts, corresponding to intersecting dispersion curves at the phase-matching point, while loss curves do not, incomplete coupling occurs. This case corresponds to Fig. 2.

To verify the independent sensing capability of the proposed sensor for refractive index and temperature, Fig. 4 presents the loss spectra under two conditions: temperature variation (with the refractive index fixed at 1.36) and refractive index variation (with the temperature fixed at 20 °C). As shown in Fig. 4(a), when the temperature changes from –20 °C to 40 °C, the loss peaks corresponding to the refractive index of 1.36 nearly overlap. This overlap indicates that the SPR channel is almost unaffected by temperature. Figure 4(b) shows that as the analyte refractive index varies

from 1.33 to 1.38, the loss peaks at 20 °C also largely overlap. Although the loss peak amplitudes vary with changes in the refractive index, the wavelength shift remains unchanged. These results confirm the relative independence between the SPR and directional coupling channels. Therefore, refractive index and temperature can be measured independently.

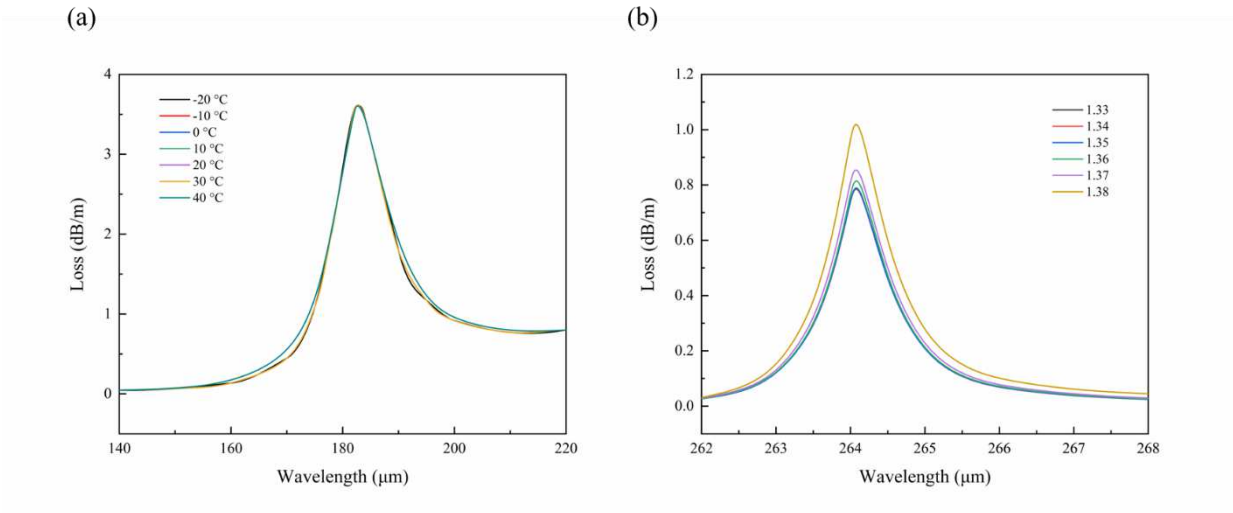


Fig.4 (a)Influence of temperature on the refractive index sensing channel;(b) Influence of analyte refractive index on the temperature sensing channel.

Effect of Design Parameters on Sensor Performances

Optimization of MoS_2 Film Thickness

Since the MoS_2 thickness t has almost no influence on the sensing characteristics of directional coupling, this paper only studies its effect on the SPR sensing channel. The lattice pitch Λ is 450 μm, and the diameters of the large and small air holes are 0.7Λ and 0.5Λ, respectively. The MoS_2 thickness is set to 6 μm, 7 μm, and 8 μm, as shown in Fig. 5(a). As t increases, the confinement loss exhibits an upward trend. This trend indicates that increasing the MoS_2 thickness enhances the SPR mode coupling between the eccentric core and the MoS_2 layer. In addition, the resonance wavelength shifts toward longer wavelengths.

The results in Fig. 5(b) show that with increasing t, both the sensitivity of the SPR channel and the FWHM increase. Although the refractive index sensitivity reaches its highest value at t=8 μm, the FWHM increases sharply. Such a sharp increase results in a poor detection limit, lower resolution, and difficulty in simultaneous multiparameter detection. Therefore, the MoS_2 thickness of 7 μm is selected as the optimal optimal parameter

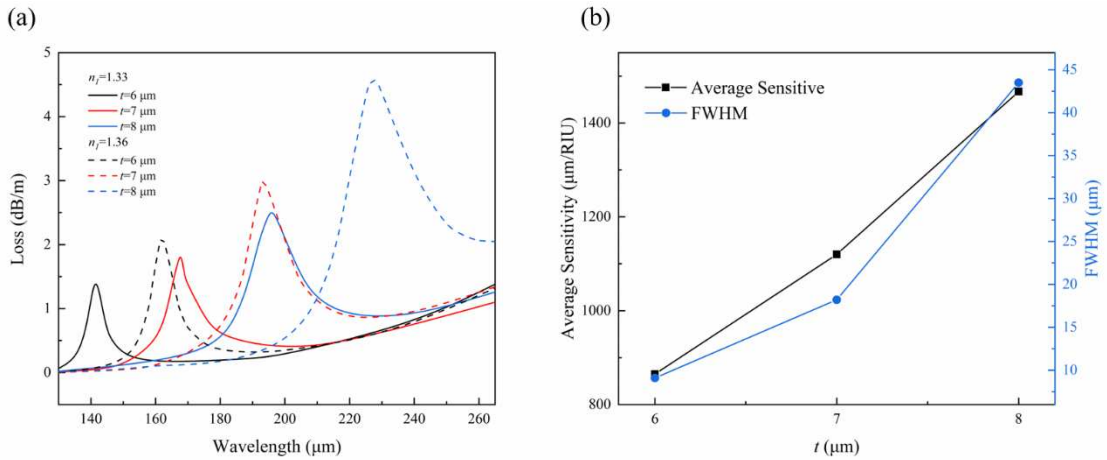


Fig.5 (a) The loss spectra of the central mode at different t values; (b) The average sensitivity and the FWHM of the loss spectrum at n_f=1.36 correspond to the different t.

Optimization of Pitch Size Λ

Figure 6 illustrates the effect of Λ on both the SPR and directional coupling channels. The thickness of the MoS_2 is kept at 7 μm. The large and small air hole diameters are set to 0.7Λ and 0.5Λ, respectively. Λ takes values of 350, 400, 450, and 500 μm.

As shown in Fig. 6(a), as Λ increases, the confinement loss of the SPR channel decreases. This trend indicates that a larger lattice pitch increases the coupling distance between the sensing layer and the eccentric core. Consequently, the mode field overlap and energy transfer between the core mode and the SPP mode weaken. The resonance wavelength first shifts to longer wavelengths and then to shorter wavelengths.

Figure 6(b) shows that both the sensitivity and the FWHM of the SPR channel first increase and then decrease as Λ rises. At Λ=450 μm, the sensitivity reaches a peak of 1120 μm/RIU. At Λ=500 μm, it drops sharply. This behavior is possibly because increasing Λ within a certain range enlarges the fiber structure and shifts the resonance wavelength to longer wavelengths. As a result, the same change in the measured refractive index causes a more significant shift in the phase matching condition, thus achieving higher sensing sensitivity. However, when Λ exceeds the optimal range, the mode field overlap and energy transfer between the eccentric core and the MoS_2 layer weaken. This weakening leads to a decrease in the loss peak and sensitivity. Therefore, the sensitivity shows a trend of first increasing and then decreasing.

Figures 6(c) and 6(d) show that the sensitivity of the directional coupling channel increases with Λ, while the FWHM remains around 1 μm. Although the directional coupling channel achieves its highest sensitivity at Λ=500 μm, the sensitivity of the SPR channel decreases significantly at this value.

Considering the sensitivity, FWHM, and fiber loss of both channels, Λ=450 μm is therefore selected as the lattice pitch.

Optimization of Large Air Hole diameter *D*

Figure 7 illustrates the influence of D on the SPR and directional coupling channels. The MoS_2 thickness t is kept at 7 μm, the lattice pitch Λ is 450 μm, and the diameter of the small air holes is 0.5Λ. The diameter of the large air holes D is set to 0.65Λ, 0.7Λ, 0.75Λ, and 0.8Λ. As shown in Fig. 7(a), as D increases, the confinement loss gradually increases, and the resonance wavelength shifts toward longer wavelengths. Figure 7(b) shows that both the sensitivity and the FWHM of the SPR channel increase with D. Although the refractive index sensitivity reaches its maximum at D=0.8Λ, the FWHM also increases significantly.

Figures 7(c) and 7(d) indicate that for the directional coupling channel, as D increases, both the fiber loss and sensitivity increase, while the FWHM decreases. While both channels exhibit peak sensitivity at D=0.8Λ, the FWHM of the SPR channel significantly increases at this point, resulting in a poor detection limit, decreased resolution, and challenges with simultaneous multi-parameter detection.

Considering the sensitivity, FWHM, and fiber loss of both channels, D=0.75Λ is finally selected as the diameter of the large air holes.

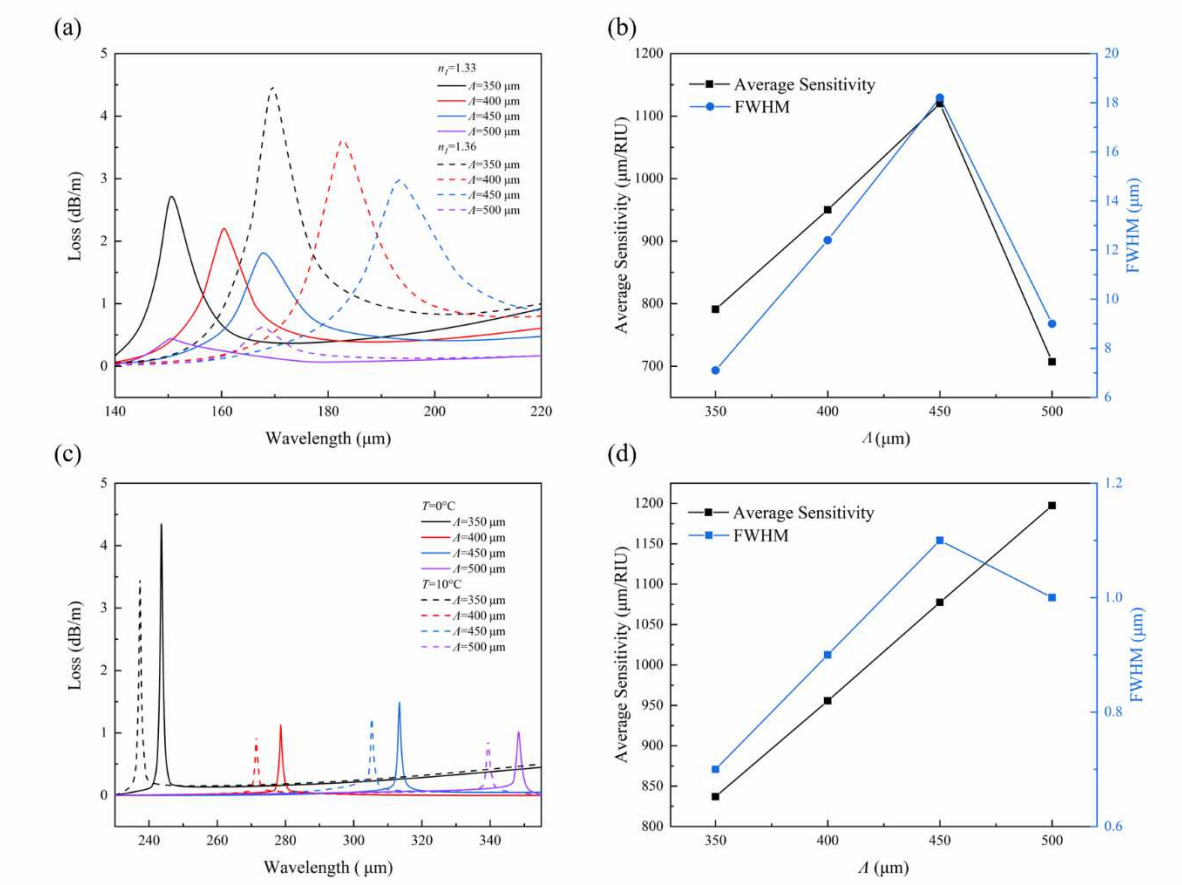


Fig.6 (a)(c) Loss spectra of SPR and directional coupling at different Λ values; (b)(d) Average sensitivity and FWHM of the loss spectra as functions of Λ at n_l=1.36 and T=10 °C

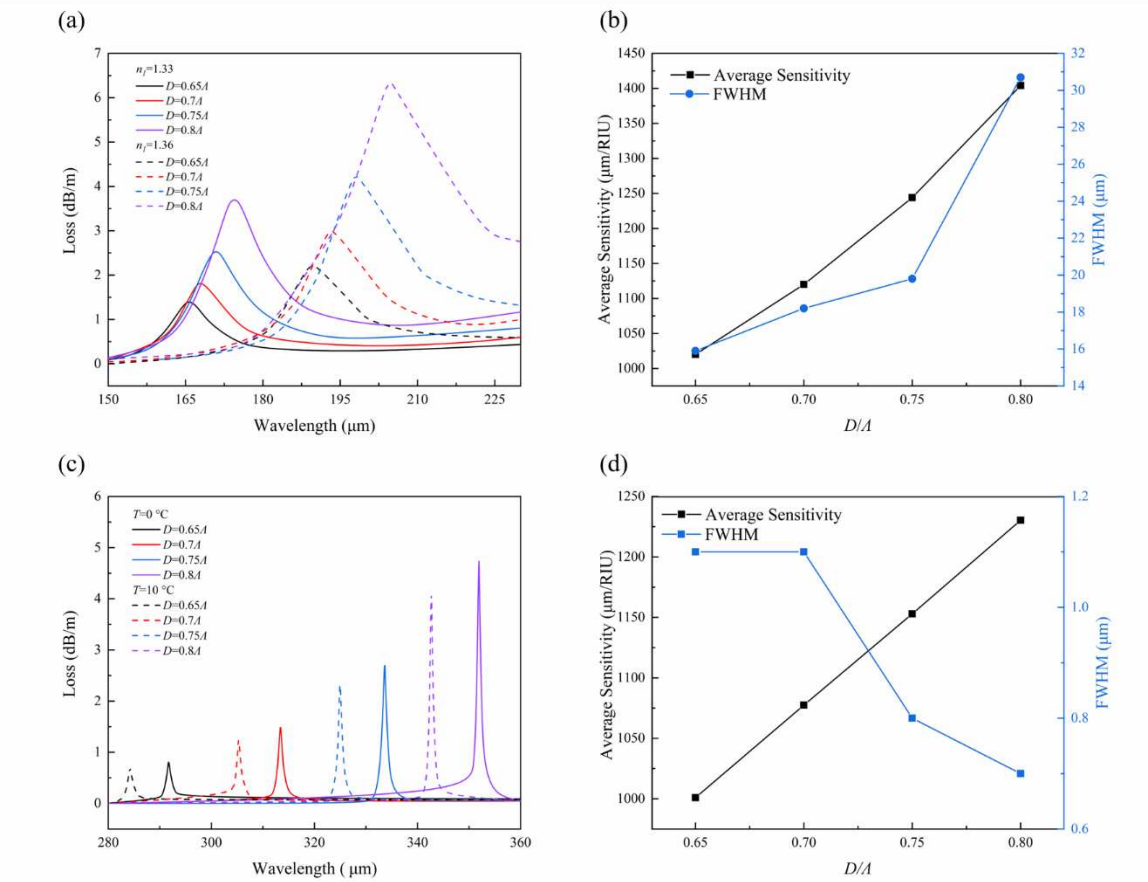


Fig.7 (a)(c) Loss spectra of SPR and directional coupling at different D values; (b)(d) Average sensitivity and FWHM of the loss spectra as functions of D at n_1=1.36 and T=10°C

Optimization of Small Air Hole diameter *d*

Figure 8 illustrates the influence of d on the SPR and directional coupling channels. The MoS_2 thickness t is kept at 7 μm, the lattice pitch Λ is 450 μm, and the diameter of the large air holes D is 0.75Λ. The diameter of the small air holes d is set to 0.3Λ, 0.35Λ, 0.4Λ, and 0.5Λ.

As shown in Fig. 8(a), as d increases, the confinement loss gradually decreases. This reduction indicates that a larger air-hole diameter enhances optical field confinement in the core, thereby reducing the evanescent-wave energy leaking to the sensing interface. Meanwhile, the resonance wavelength shifts slightly toward longer wavelengths.

Figure 8(b) shows that both the sensitivity and the FWHM of the SPR channel increase with d.

Figures 8(c) and 8(d) indicate that as d increases, the loss peak also decreases. In contrast, the sensitivity and FWHM of the directional coupling channel show an increasing trend, though with smaller increments.

At d=0.4Λ and 0.5Λ, the FWHM of the SPR channel reaches 18.2 μm and 19.8 μm, respectively. These values are much larger than the 10.7μm obtained at d=0.35Λ. Such broad linewidths limit the detection resolution. When d decreases to 0.3Λ, the sensitivity of the SPR channel decreases to 994 μm/RIU, which is not sufficient for high-sensitivity detection. Considering the sensitivity, FWHM, and fiber loss of both channels, d=0.35Λ is selected as the optimal diameter for the small air holes.

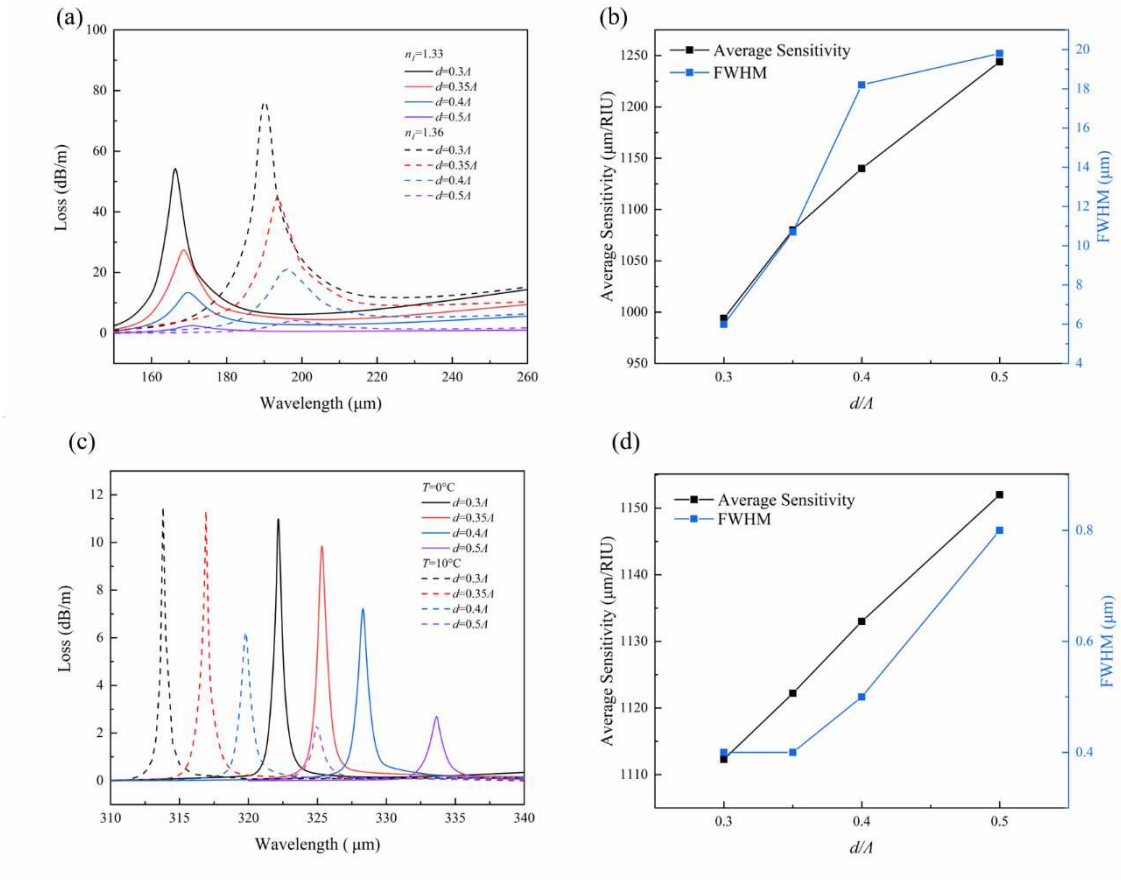


Fig.8 (a)(c) Loss spectra of SPR and directional coupling at different *d* values; (b)(d) Average sensitivity and FWHM of the loss spectra as functions of *d* at n_1=1.36 and *T*=10°C

Results and Discussion

Fig. 9(a) shows the resonance peak shifts when the temperature is 10°C, and the refractive index varies from 1.33 to 1.38 in steps of 0.01. As the analyte refractive index n_1 increases, the resonance loss peak shifts toward longer wavelengths, and the peak loss gradually increases. Figure 9(b) illustrates the relationship between the resonance wavelength and the refractive index, indicating a strong linear correlation. In the range of 1.33 to 1.38, the results of a linear regression analysis show that the refractive index sensitivity is 1080.0 μm/RIU, with a linear fit coefficient of determination (R^2) of 0.9679.

With the refractive index held constant at 1.36 and the temperature ranging from –20 °C to 40 °C, Fig. 10(a) shows the corresponding resonance peak shifts. As the temperature T increases, the resonance loss peak shifts toward shorter wavelengths, and the peak loss gradually decreases. Figure 10(b) illustrates the relationship between resonance wavelength and temperature, demonstrating a strong linear correlation. Within the temperature range of –20 °C to 40°C, linear regression analysis yields a temperature sensitivity of 0.85 μm/°C, which equates to 1122.2μm/RIU in terms of refractive index. The FWHM remains approximately 0.4 μm, and the R^2 for the linear fit is 0.99967.

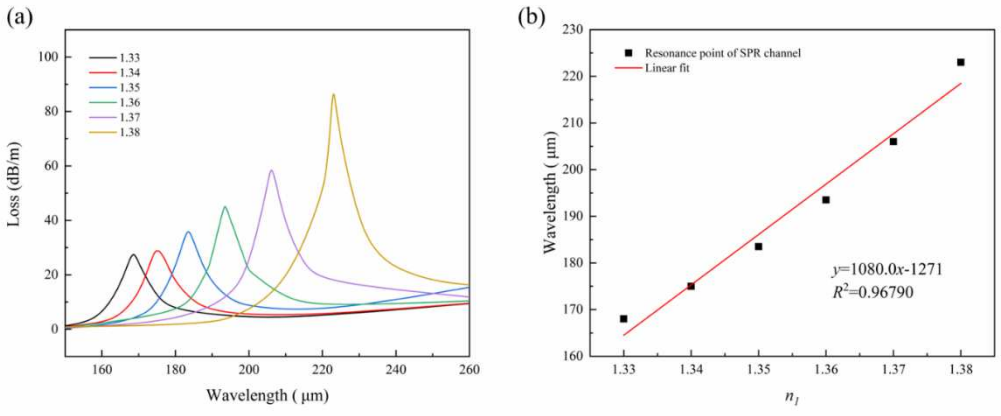


Fig.9. (a) Resonance wavelength shift for different refractive indices; (b) Linear fitting of the resonance wavelength versus refractive index

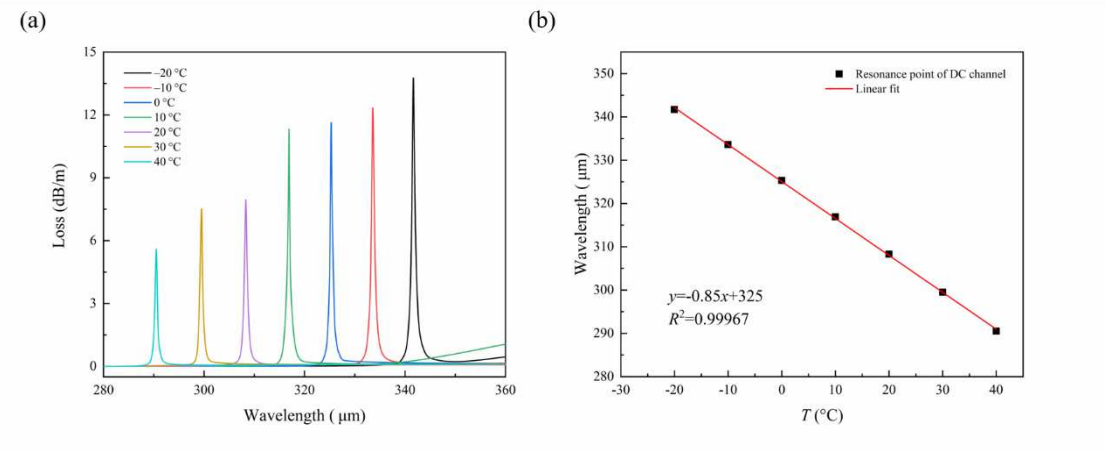


Fig.10. (a) Resonance wavelength shift for different temperatures; (b) Linear fitting of the resonance wavelength versus temperature

Tolerance analysis

Due to fabrication imperfections, the actual structural parameters of the optical fiber inevitably deviate from the design values; therefore, fabrication tolerances must be considered in the design. Following the recommendation of Paul et al. [22], we adopt a ±1% fabrication tolerance for the geometric deviation simulations. The variation ranges of the MoS_2 thickness t, lattice pitch Λ, large air-hole diameter D, and small air-hole diameter d are all set to ±1%. The analyte refractive index is fixed at 1.36, and the temperature is set to 10 °C.

Fig. 11(a) and Table1 present the influence of these structural parameter variations on the SPR channel within the tolerance range. When Λ, D, and d are set to −1%, 0% (optimal), and +1%, respectively, the resonance wavelengths of the corresponding loss curves remain nearly unchanged at n_1=1.36, with a maximum relative error of 0.31%. Although the resonance wavelength shift caused by variations in t is slightly more noticeable, the relative error is only 1.292%. Both errors fall within acceptable ranges and do not affect the sensor performance, confirming that this channel maintains good performance stability under the considered tolerances.

Fig. 11(b) and Table1 illustrate the effects of the same parameter variations on the directional coupling channel. Changes in t and d barely alter the resonance wavelength (maximum relative error of only 0.063%), and variations in t have no impact on this channel. In contrast, changes in Λ and D cause larger resonance wavelength shifts, yet the maximum relative error remains 0.685%, which is also within an acceptable range and does not impair the sensor performance.

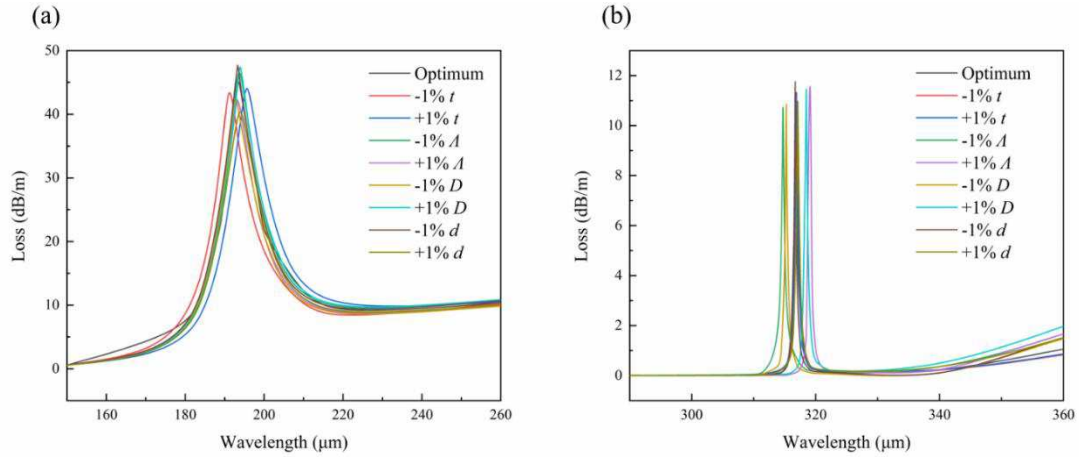


Fig.11. Confinement loss curves with ±1% fabrication tolerance: (a) SPR channel (n_1=1.36); (b) directional coupling channel (T=10 °C).

Table1 The performance parameters of the fiber optic sensor after size change.

parameter	Size change ratio	SPR channel (n_1=1.36)		Directional Coupling channel (T=10°C)	
		λ_{peak}(μm)	Relative error	λ_{peak}(μm)	Relative error
	-1%	191.0	1.292%	316.92	0%
t	Optimum	193.5	-	316.92	-
	+1%	196.0	1.292%	316.92	0%
	-1%	194.0	0.258%	314.75	0.685%
Λ	Optimum	193.5	-	316.92	-
	+1%	193.1	0.207%	319.10	0.688%
	-1%	192.9	0.310%	315.28	0.517%
D	Optimum	193.5	-	316.92	-
	+1%	193.9	0.206%	318.51	0.502%
	-1%	193.3	0.103%	316.71	0.063%
d	Optimum	193.5	-	316.92	-
	+1%	193.6	0.052%	317.13	0.066%

Note. Relative error= $\frac{\Delta\lambda_{peak}}{\lambda_{peak(Optimum)}}\times 100\%$ [9][23]

Table 2 presents a performance comparison between this sensor and representative studies in the literature. Relative to existing THz PCF-SPR dual-parameter sensors, this sensor exhibits marked improvements in sensitivity, FWHM, and resolution—specifically, sensitivity is enhanced, FWHM is narrowed, and resolution is improved. Moreover, the responses of the refractive-index and temperature channels are highly independent, enabling dual-parameter discrimination without matrix demodulation. This design offers a novel design paradigm for dual-parameter sensing that concurrently achieves high sensitivity, high resolution, and robust anti-crosstalk performance. These advantages stem from three key innovations:

Structural design: Combining an eccentric core with a directional coupling mechanism overcomes the limitations of conventional SPR-only designs. This configuration reduces the FWHM of the temperature channel to a narrow value, significantly increasing the figure of merit, while also preserving good independence between the two channels.

Material selection: MoS_2 is employed as the plasmonic material; its high specific surface area strongly enhances the surface plasmon resonance, thus boosting biosensing capability. Additionally, low-refractive-index PTFE is used as the substrate, which broadens the detection range and strikes a good balance between performance and practicality.

Fabrication process: The sensor structure is simple and does not require polishing or inter-hole coating. The MoS_2 layer can be readily deposited or transferred, and the PTFE substrate is easy to process, rendering the overall fabrication procedure more convenient and efficient.

Table2 Sensing capabilities of different PCF sensors

Reference	Ranges	Wavelength Sensitivity(μm/RIU)	FWHM(μm)	Resolution(RIU)
[9]	1.33-1.40	715.6(avg.)	14.1	1.40×10^{-7}
[11]	1.00-1.03	110(avg.)	18.0*	9.09×10^{-7}
	1.00-1.03	102.5(avg.)	-	-
[12]	1.36-1.46	153.8(max.)	-	6.5×10^{-7}
		602.5(max.)	-	1.66×10^{-7}
[13]	20-90℃	222.2(max.)	1.9*	4.5×10^{-7}
	40%-80%RH	2385.7(max.)	26.5*	4.19×10^{-8}
This Work	1.33-1.38	1080.0(avg.) 1700(max.)	10.7	9.25×10^{-8}
	-20-40℃	1122.2(avg.) 1185.1(max.)	0.4	8.91×10^{-8}

Note. Sensitivity $S_\lambda = \frac{\Delta\lambda}{\Delta n}$ (μm/RIU) ,Resolution $R = \frac{\Delta\lambda_{\min}}{S_\lambda}$ (RIU).

Suppose the instrument has a minimum wavelength resolution of 0.1nm.

***** indicates that we calculated it ourselves based on the literature

Conclusion

To address challenges such as temperature cross-sensitivity, limited sensitivity for trace detection, and insufficient probing depth for large molecules, this paper proposes a novel THz eccentric-core PCF structure for dual-parameter sensing. The sensor uses SPR from an external coating and directional coupling from a central temperature-sensitive liquid to independently detect refractive index and temperature. This approach avoids complex matrix demodulation. Simulation results show that, within a refractive index range of 1.33–1.38 and a temperature range from –20 °C to 40 °C, the sensor achieves average refractive index sensitivities of 1080.0 μm/RIU and 1122.2μm/RIU, respectively. The proposed structure combines ultra-high sensitivity, large probing depth, freedom from cross-sensitivity, and multi-mechanism synergy. Therefore, this sensor holds significant potential for applications in biochemical analysis, cell detection, and trace monitoring.

Author Contributions Conceptualization and design of the work: Yanyan Wang; Writing of the manuscript: Yanyan Wang; Formal analysis and supervision: Weihua Shi; Writing comments and suggestions: Hui Zhao and Xiling Zheng.

Funding This work is partially supported by the National Natural Science Foundation of China under Grant 61571237, and in part by the Natural Science Foundation of Jiangsu Province under Grant 20221330.

Data Availability No datasets were generated or analysed during the current study.

Declarations

Ethics Approval Not applicable.

Consent to Participate All authors agreed to participate in this investigation.

Consent for Publication All authors agreed to participate in this article.

Competing interests The authors declare no competing interests.

References

1. Oudenani A, Sonne A, Saleh CMN (2025) Simultaneous sensing of temperature and refractive index with D-shaped photonic crystal fiber infused with liquid crystal. Plasmonics 20:4159-4167. https://doi.org/10.1007/s11468-024-02515-x
2. Liu M, Leng X, Ni W, Shum PP (2024) Simultaneous and ultrasensitive measurement of refractive index and temperature based on SPR of hollow-core anti-resonant fibers. Plasmonics 19:3091-3100. https://doi.org/10.1007/s11468-024-02217-4
3. Wang L, Guo P, Zhang S, et al. (2025) A single-core dual-channel optical fiber sensor based on surface plasmon resonance for simultaneous measurement of refractive index and temperature. Plasmonics 20:9405-9414. https://doi.org/10.1007/s11468-025-02973-x
4. Hassani A, Skorobogatiy M (2008) Surface Plasmon Resonance-like integrated sensor at terahertz frequencies for gaseous analytes. Opt Express 16:20206-20214. https://doi.org/10.1364/OE.16.020206
5. Qiu H, Tian J, Gao Y, et al. (2024) Ultra-high-Sensitivity Fiber-Optic Immunosensor Based on the High-Order-Harmonic Vernier Effect for Cytokeratin 19 Fragment Detection. IEEE Sensors Journal 24:18350-18358.https:/doi.org/10.1109/jsen.2024.3385361

6. Zhu L, Wan F, Bai Y, et al. (2025) A review of photo thermal spectroscopy for gas sensing. Microchemical Journal 116716.https://doi.org/10.1016/j.microc.2025.116716
7. Zhi Y, Yu XC, Gong Q, Yang L, Xiao YF (2017) Single nanoparticle detection using optical microcavities. Advanced Materials, 29(12), 1604920.https://doi.org/10.1002/adma.201604920
8. Markelz AG (2008) Terahertz dielectric sensitivity to biomolecular structure and function. IEEE Journal of Selected Topics in Quantum Electronics,14(1), 180-190. https://doi.org/10.1109/jstqe.2007.913424
9. Liu S, Ma R, Li Y, et al. (2021) D-shaped surface plasmon resonance biosensor based on MoS_2 in terahertz band. Optical Fiber Technology 66:102631.https://doi.org/10.1016/j.yofte.2021.102631
10. He J, Wang J, Liu W, Lu X, Lv J, Yang L, et al. (2024) Photonic crystal fiber based on graphene surface plasmon resonance for high-sensitivity terahertz refractive index sensing. Journal of the Optical Society of America A 41:1279-1286. https://doi.org/10.1364/JOSAA.521774
11. Liu G, Tian F, Lu Y, et al. (2022) Zeonex-based high sensitivity dual-channel SPR optical fiber sensor for gaseous analytes in terahertz regime. Optik 255:168656.https://doi.org/10.1016/j.ijleo.2022.168656
12. Xue J, Zhang Y, Guang Z, et al. (2025) MoS_2 surface plasmon resonance based high-resolution THz biosensor using a dual D-shaped channel micro-structured fiber. Optics & Laser Technology 180:111387.https://doi.org/10.1016/j.optlastec.2024.111387
13. Yin J, Zhang Y, Li S, et al. (2026) SPR-MOF terahertz sensor for simultaneous high-sensitivity temperature and humidity sensing. Physica Scripta. https://doi.org/10.1088/1402-4896/ae3fdd
14. Lee YS, Choi H, Kim B, et al. (2021) Low-loss polytetrafluoroethylene hexagonal porous fiber for terahertz pulse transmission in the 6G mobile communication window. IEEE Transactions on Microwave Theory and Techniques 69:4623-4630. https://doi.org/10.1109/tmtt.2021.3092761
15. D'Angelo F, Mics Z, Bonn M, et al. (2014) Ultra-broadband THz time-domain spectroscopy of common polymers using THz air photonics. Optics Express 22:12475-12485. https://doi.org/10.1364/cleo_si.2014.sf1f.2
16. Fedulova EV, Nazarov MM, Angeluts AA, et al. (2012, February) Studying of dielectric properties of polymers in the terahertz frequency range. In Saratov Fall Meeting 2011: Optical Technologies in Biophysics and Medicine XIII (Vol. 8337, pp. 144-152). SPIE. https://doi.org/10.1016/j.polymertesting.2024.108674
17. Yu, B. L., Zeng, F., Xing, Q., & Alfano, R. R. (2003). Probing dielectric relaxation properties of liquid CS2 with terahertz time-domain spectroscopy. Applied physics letters, 82(26), 4633-4635.
18. Siddik MAB, Hossain MS, Paul AK, et al. (2020, June) Design and Evaluation of Liquid Filled PCF Temperature Sensor Based on SPR. In 2020 IEEE Region 10 Symposium (TENSYMP) (pp. 1795-1799). IEEE. 10.1109/tensymp. https://doi.org/10.1109/tensymp50017.2020.9230693
19. Wang Y, Li S, Li J, et al. (2019) High-sensitivity photonic crystal fiber refractive index sensor based on directional coupler. Optical Fiber Technology 49:16-21. https://doi.org/10.1016/j.yofte.2019.01.015
20. Zhao J, Chen W, Meng J, et al. (2016) Integrated flexible and high-quality thin film transistors based on monolayer MoS_2. Advanced Electronic Materials 2:1500379. https://doi.org/10.1002/aelm.201500379
21. Zhang Z, Shi Y, Bian B, et al. (2008) Dependence of leaky mode coupling on loss in photonic crystal fiber with hybrid cladding. Optics Express 16:1915-1922. https://doi.org/10.1364/oe.16.001915
22. Paul, A. K., Sarkar, A. K., Islam, M. H., & Morshed, M. (2018). Dual core photonic crystal fiber based surface plasmon resonance biosensor. Optik, 170, 400-408. https://doi.org/10.1016/j.ijleo.2018.05.131
23. Mukhopadhyay, A. K., Sarkar, S., Mukherjee, S., & Das, N. R. (2024). Optimization and characterization of a PCF-based SPR sensor for enhanced sensitivity and reliability in diverse chemical and biological applications. *Journal of the Optical Society of America B*, *42*(1), 97-104. https://doi.org/10.1364/JOSAB.537519